Journal Name

ARTICLE TYPE

Cite this: DOI: 10.1039/xxxxxxxxxx

Deciphering environment effects in peptide bond solvation dynamics by experiment and theory†

Matthias Wohlgemuth,[a] Mitsuhiko Miyazaki,[b,c] Kohei Tsukada,[b] Martin Weiler,[b] Otto Dopfer,[*c] Masaaki Fujii,[*b] and Roland Mitrić[*a]

Received Date
Accepted Date

DOI: 10.1039/xxxxxxxxxx

www.rsc.org/journalname

Most proteins work in aqueous solution and the interaction with water strongly affects their structure and function. However, experimentally the motion of a specific single water molecule is difficult to trace by conventional methods, because they average over the heterogeneous solvation structure of bulk water surrounding the protein. Here, we provide a detailed atomistic picture of the water rearrangement dynamics around the -CONH- peptide linkage in the two model systems formanilide and acetanilide, which simply differ by the presence of a methyl group at the peptide linkage. The combination of picosecond pump-probe time-resolved infrared spectroscopy and molecular dynamics simulations demonstrates that the solvation dynamics at the molecular level is strongly influenced by this small structural difference. The effective timescales for solvent migration triggered by ionization are mainly controlled by the efficiency of the kinetic energy redistribution rather than the shape of the potential energy surface. This approach provides a fundamental understanding of protein hydration and may help to design functional molecules in solution with tailored properties.

1 Introduction

The interaction of water with solutes and the formation of complex hydrogen-bonded (H-bonded) networks are important driving forces in biochemical reactions and structural rearrangements [1–7]. In particular, the structure and function of proteins is intimately connected with the dynamics of the water network. For example, protein folding and enzyme activity involve hydrogen-bond dynamics that spans multiple timescales [8–22]. With their –CONH– linkages along the peptide chain, proteins offer attractive hydrogen bonding sites, where water can bind either as proton donor at the CO site or as proton acceptor at the NH site, respectively [23].

The solvation dynamics around proteins has been probed by various experimental methods. However, the results are often inconsistent and contradictory [9,12,14,15,19,22,24]. This difficulty arises from the inherent complexity of protein solvation, such as the existence of multiple solvation layers. In such a situation, individual methods may measure water molecules in different layers. Therefore, most experiments yield only indirect dynamical information averaged over various water molecules in different local environments, giving rise to only a limited picture of the dynamics of individual water molecules [15]. Apparantly, measuring the motion of a specific single water molecule in real biological environments is a challenging experimental task [25]. One possibility to overcome these limitations is the generation of size- and isomer-selected (micro-)hydrated peptides in the gas phase and study the dynamics of a single or several selected solvent molecules with time-resolved pump-probe techniques, such as time-resolved photoelectron spectroscopy [26–29] or the recently developed picosecond time-resolved infrared (ps-TRIR) spectroscopy [25,30]. The latter one has successfully been applied to monitor in real time the ionization-induced $\pi \rightarrow$H site-switching dynamics of rare gas ligands attached to the phenol molecule [30–34] and the water migration dynamics in the 4-aminobenzonitrile-water [35] and trans-acetanilide-water ($AA^+ - W$) [36] cluster cations. Combined with theoretical simulations, such experiments provide a detailed atomistic picture of the dynamics of individual solvent molecules. Conceptually, such experiments involve the preparation of neutral clusters in a cold molecular beam in their ground electronic state (S_0), which are subsequently resonantly ionized via the first excited state (S_1) into the cation ground state (D_0) using size- and isomer-selective two-photon ionization. Ionization triggers a re-

[a] Institut für Physikalische und Theoretische Chemie, Julius-Maximilians-Universität Würzburg, Emil-Fischer-Str. 42, 97074 Würzburg, Germany. E-Mail: roland.mitric@uni-wuerzburg.de.
[b] Laboratory for Chemistry and Life Science, Institute of Innovative Research, Tokyo Institute of Technology, Yokohama 226-8503, Japan. E-Mail: mfujii@res.titech.ac.jp.
[c] Institut für Optik und Atomare Physik, Technische Universität Berlin, 10623 Berlin, Germany. E-Mail: dopfer@physik.tu-berlin.de.

† Electronic Supplementary Information (ESI) available: Movies of the water migration dynamics, REMPI spectra of FA-W.

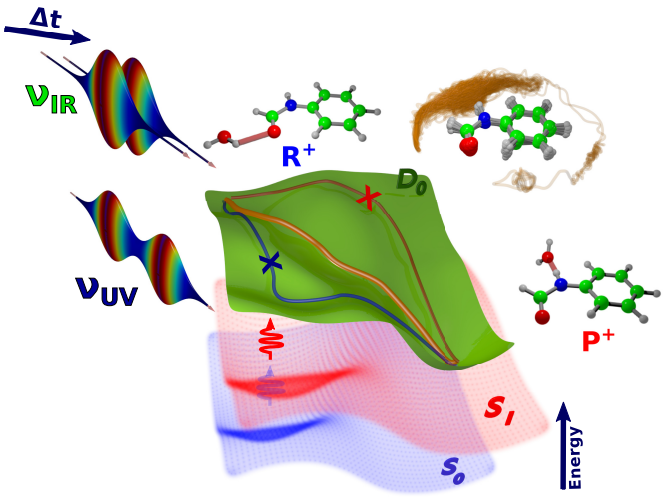

Fig. 1 Scheme illustrating the experimental pump-probe procedure and dynamical time evolution after the ionization of the trans-formanilide-water (FA – W) cluster. The CO-bound isomer is ionized by size- and isomer-selective two-color two-photon ionization, pump process) from the neutral ground state (S_0, blue surface) via the first excited state (S_1, red surface) to the cationic ground state (D_0, green surface). There, the water molecule migrates from the hydrogen-bonded CO-site ($FA^+ - W^{CO}$, R^+) to the NH-bound isomer ($FA^+ - W^{NH}$, P^+). This motion is monitored by ps-TRIR spectra (ν_{IR}) measured at variable delay Δt (probe process). The two crossed pathways indicate the migration channels of $AA^+ - W$, which are not observed in the $FA^+ - W$ MD simulations, while a new third channel (yellow trace) opens in plane (c.f. middle inset structure with traces).

sponse of the solvent to the charge redistribution, because the interaction potential in the ionized D_0 state changes drastically. As a consequence, the ligand is released from its initial binding site in the neutral cluster and undergoes an exothermic large-amplitude migration reaction toward the most attractive binding site in the cation cluster on the picosecond timescale. Tunable IR laser radiation (ν_{IR}) introduced at a variable delay (Δt) after the ionization event probes the isomerization dynamics (Fig. 1), because resonant vibrational excitation induces the dissociation of the cluster. In this way the transient time-dependent IR spectrum can be measured, and the vibrational fingerprints of the corresponding transient structures are experimentally obtained. However, to extract full information from the observed time-resolved IR spectra, high-level dynamical theoretical simulations are required[37]. To this end, we have recently introduced a new and generally applicable theoretical approach for the simulation of solvation dynamics and pump-probe ps-TRIR spectra based on ab initio molecular dynamics (MD) "on the fly", and successfully applied it to the water migration dynamics of the $AA^+ - W$ cluster, which serves as a model for solvating the peptide linkage[37]. With our approach, we were able to identify competing water rearrangement channels and to determine the timescales of the involved relaxation processes. This theoretical approach is verified by simulating the ps-TRIR spectra, which agree well with the experimental ones[36].

Here, we investigate the influence of the local environment on the solvation dynamics of a single water molecule bound to two aromatic amides, namely trans-formanilide-water (FA – W) and trans-acetanilide-water (AA – W) clusters. Notice, that although there are certainly more chemically suitable systems for modelling the solvation dynamics of a peptide bond, our choice of an aromatic model peptide is motivated by our experimental technique, which relies on the resonant ionization. The two molecules differ only by the presence of a methyl group directly bound to the peptide linkage in AA. We show that even a small perturbation in the local structure, in this case substitution of H by CH_3, can completely change both the mechanism and the timescale of the water rearrangement around the peptide linkage. Although N-methylation of peptides does not play a substantial role in proteins, it is an important matter of interest in drug design and synthesis of new nanomaterials[38–40]. In the electronic ground state of neutral FA – W, water binds with similar binding energies either as a proton acceptor to the NH site ($FA - W^{NH}$) or as a proton donor to the CO site ($FA - W^{CO}$)[41,42]. The barriers for isomerization have been determined as 892±92 cm^{-1} (CO→NH) and 869±119 cm^{-1} (NH→CO)[43]. However, in the cationic ground state (D_0), the CO site becomes repulsive and thus, as shown by recent high-resolution photoelectron (ZEKE) and IR experiments, water exclusively binds to the NH site[42,44–46]. Therefore, ionization of the $FA - W^{CO}$ cluster triggers water migration from the CO site to the now more stable NH binding site[42], as has been shown by Sekiya and co-workers by IR spectroscopy. Previous MD simulations at the Hartree-Fock (HF) and density functional theory (DFT) levels suggest water migration in $FA^+ - W^{NH}$ after vertical ionization of the $FA - W^{CO}$ isomer within a sub-picosecond timescale[42,47]. However, the role of a possible back reaction, the occurrence of reaction intermediates, and the origin of the predicted shorter lifetime compared to the related $AA^+ - W$ cluster remained unclear. Concerning higher degrees of solvation, the formation of H-bonded networks and π-bounded clusters of FA^+ with polar and nonpolar ligands have been studied by infrared photodissociation spectra and quantum chemical calculations of size-selected $FA^+ - L_n$ clusters with L=W (n=1-5), L=Ar (n=1-8), and $L=N_2$[46,48], yielding detailed information about the microsolvation shell structure of this fundamental ion in hydrophilic and hydrophobic environments.

This paper is structured as follows. First, we present the theoretical background to simulate ps-TRIR spectroscopy (section II), which is followed by the description of the employed experimental and theoretical methodology (section III). In section IV, we show the results and discuss the obtained ps-TRIR spectra. Finally, we summarize the salient results (section V).

2 Simulation of Picosecond Time-Resolved Infrared Spectroscopy

We present a detailed description of the theoretical methodology for the simulation of the ps-TRIR spectra, which is based on MD "on-the-fly" carried out in the frame of DFT. For this purpose, we employ the Wigner representation in which the density operator of the system is represented by a phase space function $\rho(\mathbf{q},\mathbf{p},t)$ of the nuclear coordinates and momenta. As in our previ-

ous work[49,50], ρ is represented by an ensemble of independently propagated discrete classical trajectories according to

$$\rho(\mathbf{q},\mathbf{p},t) = \sum_{i=1}^{N_{traj}} \delta(\mathbf{q}-\mathbf{q}_i(t;\mathbf{q}_0,\mathbf{p}_0))\delta(\mathbf{p}-\mathbf{p}_i(t;\mathbf{q}_0,\mathbf{p}_0)), \quad (1)$$

where N_{traj} is the total number of trajectories and $\mathbf{q}_0$ and $\mathbf{p}_0$ are the initial positions and momenta of the nuclei of the i-th trajectory. The Hamilton function for the system driven by a laser field is

$$H(\mathbf{q},\mathbf{p},t) = H_0(\mathbf{q},\mathbf{p}) - \mu(\mathbf{q})\cdot\mathbf{E}(t), \quad (2)$$

with the field-free Hamiltonian H_0 and the coupling to the external laser field $\mathbf{E}(t)$ through the total dipole moment $\mu(\mathbf{q}) = \mu_N(\mathbf{q}) + \mu_e(\mathbf{q})$, which is composed of the nuclear and electronic contributions, respectively. We treat the interaction with the field as a weak perturbation. The time evolution of the phase space density in the classical limit of the Wigner representation is described by the Liouville equation

$$\dot{\rho} = \{H,\rho\} = \sum_{i=1}^{3N} \frac{\partial H}{\partial q_i}\frac{\partial \rho}{\partial p_i} - \frac{\partial H}{\partial p_i}\frac{\partial \rho}{\partial q_i}, \quad (3)$$

where $\{H,\rho\}$ is the classical Poisson bracket of the Hamilton function (Eq. (2)) and the phase space density (Eq. (1)). The solution of this equation is equivalent to the solution Hamiltons equations of motion for the functions $q_i(t)$ and $p_i(t)$:

$$\dot{q}_i = \frac{\mathrm{d}H}{\mathrm{d}p_i} \quad (4)$$

$$\dot{p}_i = -\frac{\mathrm{d}H}{\mathrm{d}q_i} = -\frac{\partial V}{\partial q_i} + \frac{\partial \mu}{\partial q_i}\cdot\mathbf{E}(t). \quad (5)$$

The forces acting on the nuclei are $\frac{-\partial V}{\partial q_i} = F_i$ and are obtained as gradients of the electronic potential energy surface $V(\mathbf{q})$. In the 0-th order of perturbation, which can be employed for weak laser fields, the last term of Eq. (5) can be neglected, and therefore the phase space ensemble can be propagated freely using quantum chemical MD "on the fly". For this purpose, we utilize analytic energy gradients, which can be efficiently calculated with DFT and are employed for the numerical integration of the equations of motions (4) and (5). In order to simulate time-resolved pump-probe IR spectra, we have to consider two interactions with the laser field, separated by the time delay Δt: (1) the interaction with the UV pump laser pulse centered at $t = 0$ ionizes the neutral cluster and populates the cationic state, and (2) the dynamics in the cationic state is probed by an IR laser pulse centered at the time delay Δt with the Gaussian shape:

$$\mathbf{E}(t) = \mathbf{E}_0 \exp\left(-\frac{(t-\Delta t)^2}{2\sigma^2}\right)\cos\omega t, \quad (6)$$

with the amplitude $\mathbf{E}_0$ and σ the width of the laser pulse. The rate of the energy absorption induced by the interaction with the probe laser is calculated in the phase space representation from the statistical average of the internal energy $\langle E\rangle$:

$$\begin{aligned}\frac{\mathrm{d}\langle E\rangle}{\mathrm{d}t} &= \frac{\mathrm{d}}{\mathrm{d}t}\iint \mathrm{d}\mathbf{p}\mathrm{d}\mathbf{q}\, H_0(\mathbf{q},\mathbf{p})\rho(\mathbf{q},\mathbf{p},t) \\ &= \iint \mathrm{d}\mathbf{p}\mathrm{d}\mathbf{q}\, H_0(\mathbf{q},\mathbf{p})\{H,\rho\}, \end{aligned} \quad (7)$$

where we use the Liouville equation of motion for the phase space density (Eq.(3)). By expanding the Poisson bracket and using partial integration, Eq. (7) can be reduced to

$$\begin{aligned}\frac{\mathrm{d}\langle E\rangle}{\mathrm{d}t} = \iint \mathrm{d}\mathbf{p}\mathrm{d}\mathbf{q} \Bigg[\rho(\mathbf{q},\mathbf{p},t)\frac{\mathrm{d}\mu(\mathbf{q}(t))}{\mathrm{d}t} \\ \times \mathbf{E}_0 \exp\left(-\frac{(t-\Delta t)^2}{2\sigma^2}\right)\cos\omega t\Bigg]. \end{aligned} \quad (8)$$

The total absorption of energy for a given frequency ω and time delay Δt, which corresponds to the experimental measured transient ps-TRIR spectrum, can be calculated by integrating the rate of energy absorption (Eq. (8)) over time

$$\langle S_{probe}(\omega,\Delta t)\rangle = \int_{-\infty}^{\infty} \mathrm{d}t \frac{\mathrm{d}\langle E\rangle}{\mathrm{d}t}. \quad (9)$$

By utilizing the representation of the phase space density by classical trajectories given in Eq. (1), this reduces to the following expression for the transient ps-TRIR spectrum for the time delay Δt:

$$\begin{aligned}\langle S_{probe}(\omega,\Delta t)\rangle = \sum_{i=1}^{N_{traj}} \int_{-\infty}^{\infty} \mathrm{d}t \Bigg[\frac{d\mu(\mathbf{q}_i(t,\mathbf{q}_0,\mathbf{p}_0))}{dt} \\ \times \mathbf{E}_0 \exp\left(-\frac{(t-\Delta t)^2}{2\sigma^2}\right)\cos\omega t\Bigg]. \end{aligned} \quad (10)$$

Note that this expression can be interpreted as a trajectory average of the windowed Fourier transform of the dipole derivative function of each trajectory, where the probe pulse envelope serves as a window.

In order to take also the pump pulse width into account, the transient IR spectra are convoluted by the change in the population of the cationic state, which is obtained directly from the experiment. This leads to the following final expression for the simulation of the ps-TRIR spectra

$$\langle S_{pump-probe}(\omega,\Delta t)\rangle = \int_{-\infty}^{\infty} \mathrm{d}t\, \langle S_{probe}(\omega,\Delta t - t)\rangle \frac{\mathrm{d}P(t)}{\mathrm{d}t} \quad (11)$$

where $\frac{\mathrm{d}P(t)}{\mathrm{d}t}$ is the rate of change of the cationic state population, which for the case of a Gaussian-shaped pump pulse is an error function.

3 Methods

3.1 Experimental Setup

The principle and apparatus of ps-TRIR spectroscopy have been described elsewhere[25,30,31,51,52]. Briefly, FA – W is ionized via the S_1 - S_0 origin band[41,43,53–55] by picosecond ultraviolet pulses, ν_{exc} and ν_{ion}. The population of $FA^+ - W$ is monitored using a quadrupole mass spectrometer[56]. A picosecond tunable IR pulse,

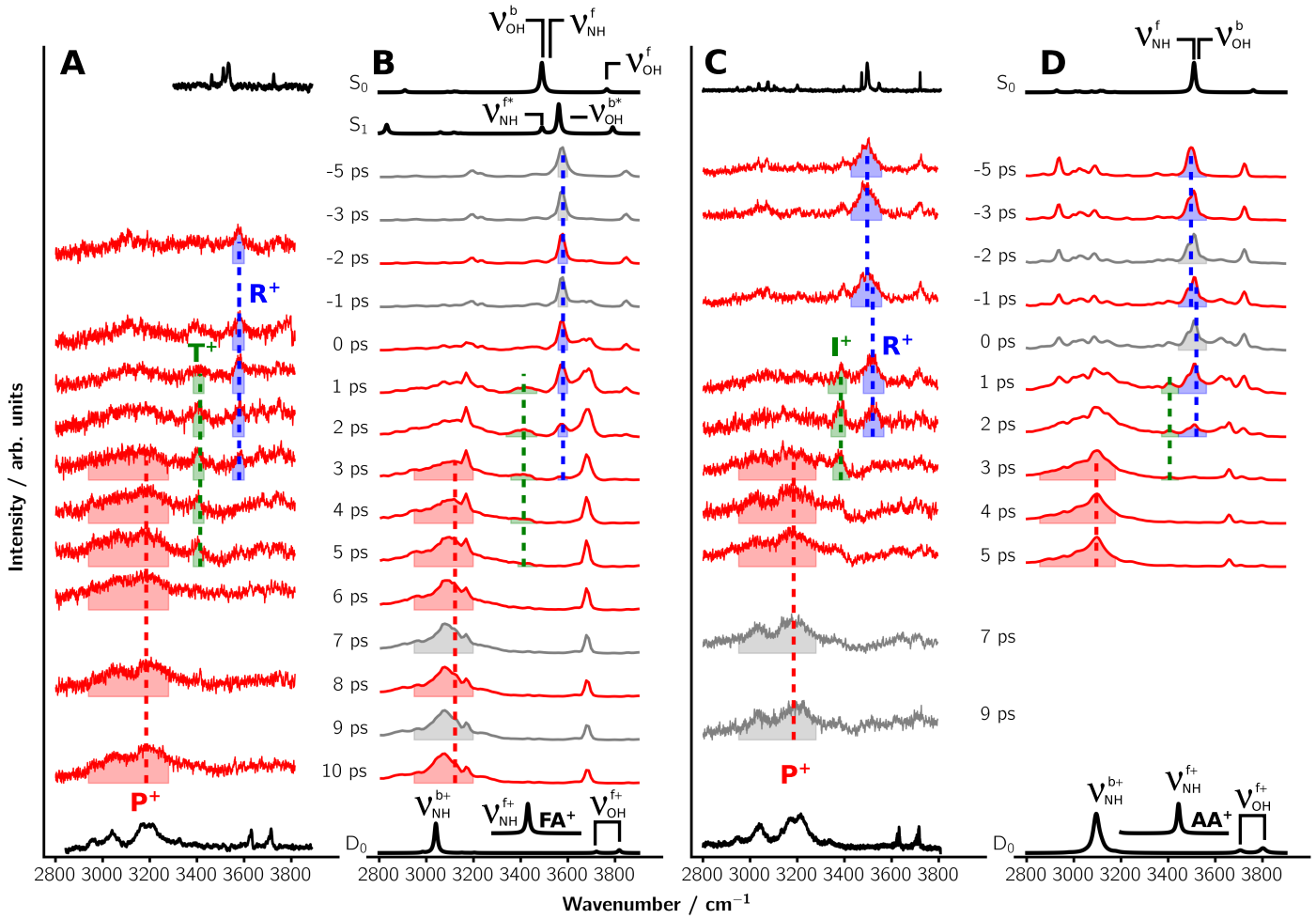

Fig. 2 ps-TRIR spectra of $FA^+ - W$ from experiment (A) and MD simulations (B) compared to ps-TRIR spectra (C,[36]) and MD simulations (D,[37]) of $AA^+ - W$. The S_0, S_1 and D_0 spectra are stationary IR spectra of the CO-bound (S_0, S_1) and NH-bound (D_0) isomers in the neutral and cationic states determined by nanosecond lasers (A[42], C) and DFT harmonic frequency calculations for the optimized structures (B, D). The inset in the D_0 spectra shows the NH stretch mode for bare FA^+ and AA^+. The highlighted areas indicate the signals uniquely attributed to the CO-bonded isomer (blue, R^+), the intermediate or transient structure (green, I^+/ T^+), where water is bound neither to the NH nor the CO site, and the NH-bound geometry (red, P^+). The gray shaded spectra denote signals which are not recorded within the experiment or are out of scope of the simulation time, respectively.

ν_{IR}, is introduced at a certain delay time (Δt) after ν_{ion} and scanned over the 3 μm range. Vibrational transitions are measured as a decrease of the monitored ion current due to vibrational predissociation of $FA^+ - W$. The time evolution of an IR transition is measured by scanning Δt while fixing ν_{IR} to this particular transition. A femtosecond mode-locked Ti:sapphire laser is regeneratively amplified and stretched to a picosecond pulse. The amplified 800 nm output is separated into three pulses. One of these pulses is frequency doubled to pump two independent optical parametric generator/amplifiers. Signal pulses from these amplifiers are frequency doubled and used as ν_{exc} and ν_{ion}. The second 800 nm pulse is used to pump another parametric generator/amplifier. Then, ν_{IR} is produced by difference frequency generation between the second harmonic of the idler output and the remaining fundamental 800 nm pulse in a KTA crystal. The typical pulse width is $\sim$3 ps, while the energy resolution is $\sim$15 cm^{-1}. These pulses are combined coaxially by beam combiners and focused on the ionization region by a lens. The frequency of ν_{ion} is set to 32250 cm^{-1} (310 nm). Vapor of FA and water is seeded in He gas, and the mixture is expanded into the vacuum chamber through a pulsed valve at a typical stagnation pressure of 1-2 bar. FA is located just behind the valve and heated to $\sim$343 K, while the water vapor is supplied from a vessel cooled down to $\sim$243 K. The clusters in the jet expansion interact with the laser pulses at $\sim$1 cm downstream from the valve, and the resultant ions are deflected toward the quadrupole mass filter by an electric field. The ion current is amplified and integrated by a digital boxcar to store the signal in a personal computer. The system is operated at 10 Hz. The conditions of the jet expansion and cluster formation are checked by resonance enhanced multiphoton ionization (REMPI) spectroscopy of $FA - W$ measured by picosecond and nanosecond pulses. The latter are obtained by frequency doubling of a Nd:YAG pumped dye laser. Typical REMPI spectra are provided in Figure S1 in the supporting information.

3.2 Computational Methodology

Throughout this work, all single-point calculations are carried out in the frame of DFT. We employ the gradient-corrected Perdew-Burke-Ernzerhof (PBE) functional[57,58] as implemented in the Turbomole program package[59], as well as the long-range corrected TD-CAM-B3LYP functional[60] as implemented in the Gaussian09 program package[61], combined with the resolution-of-identity (RI) approximation in order to speed up the MD simulations. As basis set we use the valence triple zeta plus polarization (6-311G**) basis set[62]. Grimme's dispersion correction (D3) is used throughout the simulations[63].

In order to generate the initial conditions for the MD simulations of $FA-W$ in the D_0 state, we have run a 50 ps long trajectory in the S_1 state at a constant temperature of T = 100 K employing the TD-CAM-B3LYP functional[60]. This temperature is chosen to reproduce the experimental excess energy after photoionization and is the same as the one used for the $AA-W$ simulations[37]. After initial equilibration, we have sampled structures and velocities in regular time intervals, thus generating an ensemble of 40 trajectories, which are employed to investigate the isomerization and to simulate the ps-TRIR spectra.

The MD simulations starting from these initial conditions are propagated for 10 ps forward in the D_0 cationic state and for 5 ps backward in the S_1 excited state. The integration of the classical equations of motions (Eqs. (4) and (5)) is performed using the velocity Verlet algorithm[64] with a time step of 0.2 fs, which is sufficiently small to obtain adequate conservation of energy. At each step of the trajectories, electronic and nuclear dipole moments are calculated in order to serve as basis for simulating the ps-TRIR spectra according to Eq. (10). As probe pulse, we use a Gaussian-shaped laser pulse envelope with a full-width-at-half-maximum (FWHM) of 3 ps. The rise of the population of the cationic state in Eq. (11) is modeled by a Gaussian-shaped function with a FWHM of 2.88 ps. The pump and probe pulse widths both correspond to the experimentally determined values. The transient ps-TRIR spectra are calculated in delay intervals from -5 to +10 ps according to Eq. (11).

The details for the corresponding $AA-W$ simulations are presented elsewhere[37], and are mostly the same as for the $FA-W$ simulations, except for the shorter propagation in the cationic state.

4 Results and Discussion

In Figure 2, we compare the experimental and simulated pump-probe ps-TRIR spectra monitoring the migration process of water after photoionization of $FA-W^{CO}$ (Fig. 1) with the migration process in AA^+-W[36,37]. The coarse structure of the experimental nanosecond (stationary) and ps-TRIR spectra of FA^+-W and AA^+-W are similar. The vibrational and isomer assignments of the stationary IR spectra of both clusters are presented in detail elsewhere[42,46,65]. Similarly, the ps-TRIR spectra and their interpretation based on the MD simulations in AA^+-W are detailed in[36,37]. In AA^+-W, the water molecule is released from the CO site upon ionization, and migrates to the NH site over the molecular plane. The coexistence of two channels, namely a fast one over the amide group (∼1 ps, 70%) and a slow one over the phenyl ring (∼5 ps, 30%), are identified when the observed ps-TRIR spectra are compared to the MD simulations.

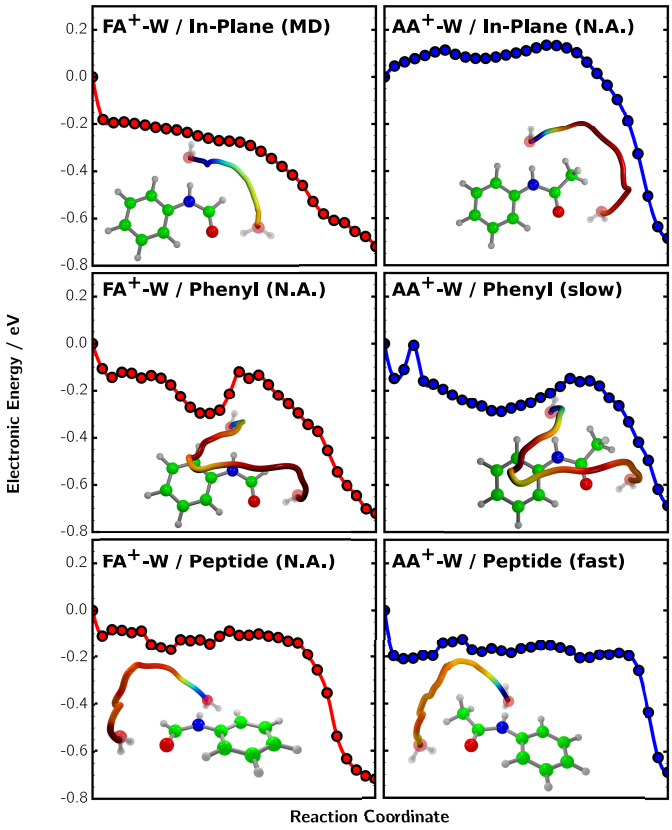

Fig. 3 Minimum energy paths derived from the nudged elastic band method of $FA-W^+$ (left) and $AA-W^+$ (right) for the migration of water from the CO to the NH site along the in-plane path (top row), above the phenyl ring (middle row), and above the peptide bond (bottom row). The insets illustrate the path of water, whereby the color encodes the energy at the point of the path. N.A. indicates the pathways not detected by the experiment and the simulations.

In Fig. 2A the experimental ps-TRIR spectra monitoring the migration process in FA^+-W are shown. The vibrational assignments are analoguous to those of AA^+-W[36]. The intensity of the H-bonded OH stretching band (ν_{OH}^{b+}) of the initially formed FA^+-W^{CO} isomer (R^+, blue) gradually decreases, followed by the formation and subsequent decrease of the free NH stretching transition (ν_{NH}^{f+}, T^+, green). At the same time, the H-bonded NH stretching band (ν_{NH}^{b+}) of the FA^+-W^{NH} reaction product (P^+, red) rises. Compared to the ps-TRIR spectra of AA^+-W (Fig. 2C[36]), the water migration process seems to be slowed down somewhat in the case of FA^+-W, which is counterintuitive since FA^+-W is a smaller system with less steric hindrance. While in the AA^+-W spectra the ν_{OH}^{b+} band (blue) has completely disappeared within 2 ps, it is still observable until 3 ps in the FA^+-W spectra. At ∼4 ps the ν_{NH}^{f+} band (green) characteristic for a locally trapped intermediate has almost disappeared for AA^+-W. In the case of FA^+-W, the ν_{NH}^{f+} band (green, T^+) still coexists with the ν_{NH}^{b+} band (red, P^+) of the FA^+-W^{NH} product and disappears only after ∼5 ps. The simulated ps-TRIR spectra of FA^+-W shown in Fig. 2B are in good agreement with the ex-

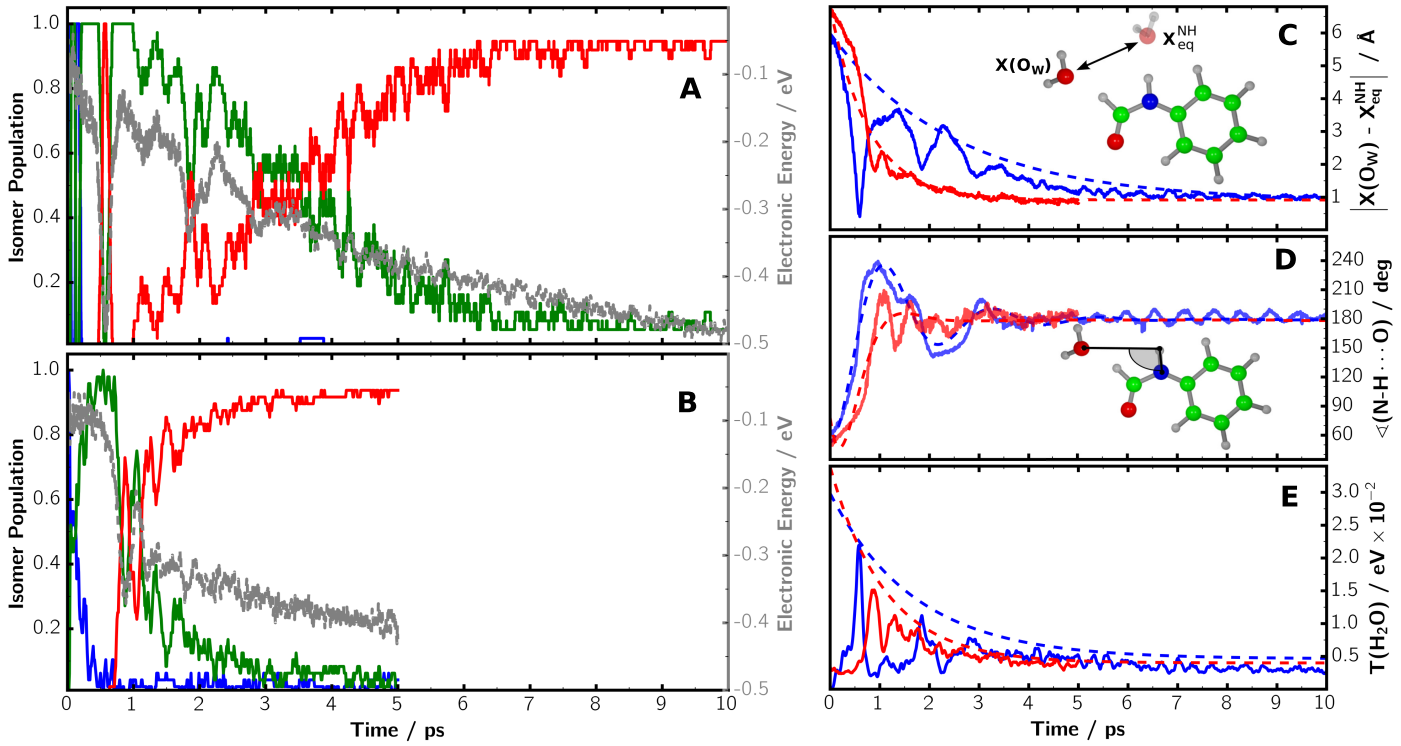

Fig. 4 Left panels: Averaged populations of the FA^+-W (A) and AA^+-W (B) ensembles, with the CO-bound isomer (blue), the transient or intermediate structure (green), and the NH-bound isomer (red) as a function of simulation time. The gray dashed line shows averaged electronic energy from the MD simulations. Right panels: (C) Averaged distance of the water oxygen (O_W) from its NH-bound equilibrium geometry, (D) averaged angle between the N-H bond of the peptide and O_W, and (E) averaged kinetic energy of water along the trajectories of FA^+-W (blue) and AA^+-W (red). The dashed lines in (C) and (E) are exponential fits with respect to the maxima of the curves. For (D) a damped harmonic oscillator was fitted to the curve.

perimental ones (Fig. 2A). Compared to the spectra simulated for AA^+-W (Fig. 2D), one can notice a more pronounced signal of the ν_{NH}^{f+} band (green). The combined experimental and theoretical approach applied to AA^+-W has shown that this band can be uniquely attributed to the existence of a slow migration channel, in which water is trapped in a local minimum above the phenyl ring and thus forms a π-bound intermediate state (I^+) responsible for the appearance of the ν_{NH}^{f+} band. As we discuss below, this pathway is completely absent in the case of FA^+-W, and the band assigned to the free NH stretch vibration (ν_{NH}^{f+}) has its origin in an in-plane large-amplitude motion of water around its final equilibrium position at the NH site. Thus, we assign this band not to an intermediate but to a transient band (T^+) of FA^+-W.

To explain these findings, we have first optimized the minimum energy paths along three different reaction coordinates from the CO-bound to the NH-bound isomer of FA^+-W and AA^+-W (Fig. 3). The two out-of-plane paths (across the peptide linkage and above the phenyl ring), which were found by the MD simulations of AA^+-W, are similar for both clusters (Fig. 3 second and third row). Additionally, we have optimized the in-plane pathway for both clusters, which was not observed in the AA^+-W simulations. Significantly, in the case of FA^+-W this path along the H atom of the amide bond is steeply descending. In contrast, in the case of AA^+-W this channel along the methyl group is blocked by a high and broad potential barrier. ZEKE photoelectron experiments assigned with CASSCF calculations find the intermolecular in-plane bending mode at 73 and 49 cm^{-1} for AA^+-W^{NH} and FA^+-W^{NH}, respectively, confirming our findings that the methyl group makes the potential energy surface stiffer along the in-plane bending coordinate and thus enhances steric repulsion[44,66]. Due to the existence of a new favorable reaction coordinate, which is even steeper and shorter than the other two found for AA^+-W, faster water migration is expected for FA^+-W.

Indeed, by monitoring the isomer population of FA^+-W (Fig. 4A), all water molecules reach the NH site for the first time within the first 500 fs after photoionization, while in the case of AA^+-W (Fig. 4B) about 70% of the water molecules first appear at 1 ps at the NH site. This difference is a consequence of the presence of a new migration channel opened by $CH_3 \rightarrow H$ substitution. The out-of-plane pathways, especially the slow migration channel with the locally trapped intermediate, as observed in the AA^+-W MD simulations (Fig. 5, right), are completely absent in the FA^+-W dynamics. Instead, all water molecules follow the steeply descending in-plane pathway (Fig. 5 left and Fig. 3 left).

But why is this migration dynamics not reflected in the ps-TRIR spectra? Instead of a fast migration and a clear appearance of the product band after 500 fs, we observe a strong absorption by the free NH stretching mode accompanied by a slow formation of the H-bonded product band. After the first arrival at the NH site, the

water molecules overshoot to the phenyl ring and start to oscillate within a large-amplitude in-plane motion forward and backward around their final equilibrium position (Fig. 5 left), also returning close to their initial position for a short time. This damped oscillation is the reason for the longer persistence of the reactant signal (R^+, blue) and the simultaneous formation of the product (P^+, red) and transient bands (T^+, green) in the ps-TRIR spectra (Fig. 2). Only the theoretical simulations reveal and illustrate the profound influence of the local environment on the dynamical pathways.

In order to analyze the relaxation process that stabilizes the water migration at the product, we present in Fig. 4 three quantities as a function of simulation time for FA^+-W (blue) and AA^+-W (red): (i) the distance of water to the NH-bound equilibrium geometry (Fig. 4C), (ii) the angle spanned by the N-H bond and the oxygen atom of water (O_W, Fig. 4D), and (iii) the kinetic energy of water (Fig. 4E). Immediately after photoionization, the internal energy is quickly transferred into translational energy of water. As can be seen from Fig. 4E, this process is about twice as fast in FA^+-W^{CO} ($\sim$500 fs) than in AA^+-W^{CO} ($\sim$1 ps), due to the steep potential directed into the in-plane motion of water (cf. top left of Fig. 3). At the moment when water approaches the NH site for the first time, the translational and vibrational energy of water is more quickly redistributed and transfered to AA^+ than to FA^+ via intracluster vibrational energy redistribution (IVR). The additional methyl group in AA^+ substantially increases the density of states by internal rotation and thus enhances the IVR rate, which can also evidently be seen from the final structures of the MD simulations (Fig. 5 bottom row). Notice, that in FA^+-W the phenyl ring provides bath modes, much in the same way as a polypeptide system with a longer backbone. In this sense it affects the IVR dynamics but not the mechanism. In AA^+-W one minor pathway (the slow one) goes over the phenyl ring and affects the overall dynamics of this pathway. However, it will not affect the $H \rightarrow CH_3$ substitution effect at the amide bond.

To quantify the difference in the effective IVR rate, the maxima of the curves in Fig. 4C and Fig. 4E are fitted to exponentially decaying functions $f(t) = f_0 \exp(-t/\tau)$. The obtained damping constants are $\tau_{C,FA} = 2.34$ ps and $\tau_{E,FA} = 1.71$ ps for FA^+-W (blue dashed line) and $\tau_{C,AA} = 1.10$ ps and $\tau_{E,AA} = 1.11$ ps for AA^+-W (red dashed line). The curves in Fig. 4D are fitted by a damped harmonic oscillator model $f(t) = f_0 \exp(-t/\tau)\cos(\omega t - \phi) + f_{off}$, where f_0, f_{off}, ω and ϕ are free parameters, giving rise to damping constants $\tau_{D,FA} = 1.36$ ps for FA^+-W (blue dashed line) and $\tau_{D,AA} = 0.46$ ps for AA^+-W (red dashed line). Thus, by averaging over all derived time constants, we determine an approximate increase in the overall IVR rate of about a factor of 2.2 for AA^+-W (with respect to FA^+-W), which is also in good agreement with the timescales determined from the experimental and theoretical ps-TRIR spectra. As it is evident from Fig. 5 the translational kinetic energy of water is rapidly transfered to FA^+ and AA^+, respectively, as soon as it reaches the NH-bound site. However, due to the different migration pathways distinct modes are excited in both molecules. In the case of AA^+-W, the out-of-plane migration leads to an excitation of the dihedral degrees of freedom of the peptide linkage and the methyl rotation. In contrast, in FA^+-W the in-plane pathway of water weakly couples to the vibrational modes of FA^+ due to the rigid in-plane bend mode of the peptide linkage and the lack of a methyl rotor, leading to a less efficient energy redistribution.

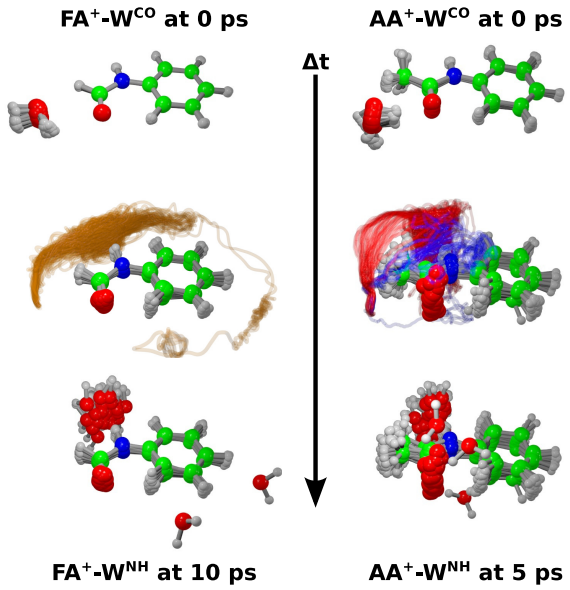

Fig. 5 Trajectories of the ionization-induced water migration derived from the FA^+-W (left, 40 trajectories) and AA^+-W (right, 50 trajectories) MD simulations, starting from the CO-bound isomer (top row) and ending at the NH-bound isomer (bottom row) at 10 ps and 5 ps after ionization, respectively. The yellow curve for FA^+-W indicates the in-plane migration path of water. The out-of-plane pathways for AA^+-W correspond to the slow (blue) and fast (red) migration channels, respectively[37].

In Fig. 6 we show the peak width of the product band (P^+, red) of the simulated ps-TRIR spectra (Fig. 2B and 2D) located between 3000 and 3300 cm^{-1}, which serves as an indicator for cooling by IVR. The broadness of the band sharpens twice as fast for AA^+-W as compared to FA^+-W. These results clearly show that, due to the stronger coupling of the isomerization coordinate to the dihedral degrees of freedom of the peptide linkage (i.e., the angle between the phenyl and amide planes) and the additional density of states of the AA^+-W cluster introduced by CH_3 substitution, IVR is more efficient for the out-of-plane pathways in the AA^+-W migration dynamics than the in-plane pathway in FA^+-W. These factors give rise to a twice longer relaxation time in FA^+-W, although the simple migration process up to the first arrival at the NH site is twice as fast compared to the AA^+-W migration dynamics.

5 Conclusions and outlook

In conclusion, we have provided a detailed atomistic picture of the strongly different water rearrangement dynamics around the peptide linkage in two model systems, which differ by the local environment around the amide moiety (by simple $H \rightarrow CH_3$ substitution). In contrast to AA^+-W with two competing out-of-plane pathways (fast and slow), the water migration dynamics in FA^+-W has only a single in-plane reaction pathway, which involves a damped large-amplitude vibrational motion around the

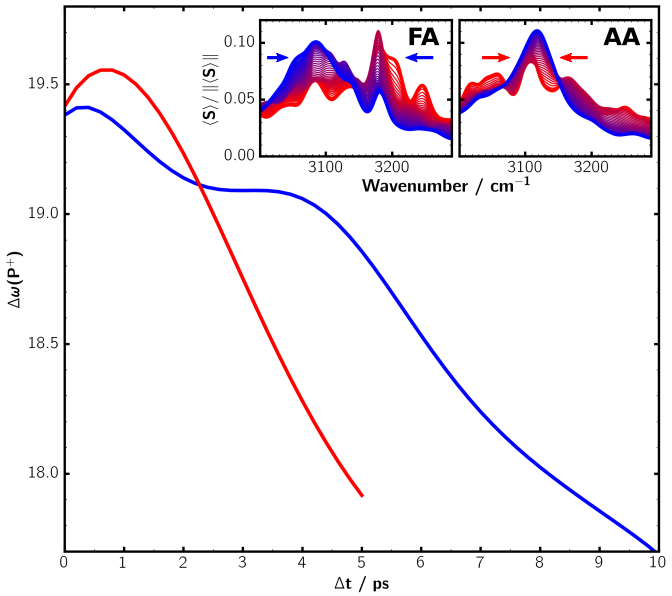

Fig. 6 Average peak width $\Delta\omega$ of the product band (ν_{NH}^{b+}, P^+) calculated for $FA^+ - W$ (blue) and $AA^+ - W$ (red) from the simulated ps-TRIR spectra (Fig. 2B and 2D). The peak width has been calculated as $\Delta\omega = (\omega_2 - \omega_1)^{-1} \int_{\omega_1}^{\omega_2} d\omega \left[\langle\omega^2\rangle - \langle\omega\rangle^2\right]^{\frac{1}{2}} \frac{\langle S(\omega,\Delta t)\rangle}{\|\langle S(\omega,\Delta t)\rangle\|}$, with $\omega_1 = 3000\ cm^{-1}$ and $\omega_2 = 3300\ cm^{-1}$. The insets show the normalized band of $FA^+ - W$ and $AA^+ - W$, respectively.

single H atom of the amide. The two out-of-plane pathways observed in $AA^+ - W$ are completely absent in the $FA^+ - W$ dynamics. The initial formation of the NH-bound isomer is twice faster in $FA^+ - W$ and completed within 500 fs, whereas in the $AA^+ - W$ trajectories only about 70% of the water molecules reach the NH site within ~1 ps via the fast channel. However, our calculations have shown that in $AA^+ - W$ the kinetic energy of water along the reaction coordinate is redistributed much faster to AA^+ than in $FA^+ - W$, which leads to faster product stabilization in the cluster with larger steric hindrance ($AA^+ - W$). The residual energy of water in $FA^+ - W$ leads to an overshooting from the equilibrium position and a long-lasting large-amplitude oscillation in the molecular plane before settling at the final NH binding site, as a result of weak coupling of in-plane intermolecular bend (with very low frequency of 49 cm^{-1}) to other vibrational modes. The consequence is a long persistence of the free NH (ν_{NH}^{f+}) stretching band in the ps-TRIR spectra of $FA^+ - W$. Our results demonstrate that the solvation dynamics at the molecular level can be strongly influenced even by small structural perturbations and that the effective timescales extracted from the time-resolved experiments are determined by the IVR rate and do not necessarily reflect the intrinsic rate of the product formation, which is mainly determined by the shape of the potential energy surface.

Since our method is generally applicable and provides an accurate and efficient way to simulate time-resolved infrared spectroscopy, which is directly comparable to the experimental outcome, a wide variety of applications are conceivable and planned for future work. For example, it will be interesting to study migration and rearrangement dynamics of the presented biomolecules with more than one water molecule, as has been studied experimentally before by stationary spectroscopic experiments[46]. The work on such simulations is currently in progress.

Acknowledgments

This work was supported in part by KAKENHI (JP205104008) on innovative area (2503), KAKENHI (JP15H02157, 384 JP15K13620, JP16H06028) and the Cooperative Research Program of the "Network Joint Research Center for Materials and Devices" from the Ministry of Education, Culture, Sports, Science and Technology (MEXT), Japan, the Core-to-Core Program (22003) from the Japan Society for the Promotion of Science (JSPS), and the Deutsche Forschungsgemeinschaft (DFG DO 729/4, ENPMI-1236). Financial support by the European Research Council (ERC) Consolidator Grant "DYNAMO" (Grant No. 646737) is gratefully acknowledged. M.M. is grateful for a fellowship from the Alexander von Humboldt foundation (research fellowship for experienced scientists). O.D. is grateful for travel support from the World Research Hub Initiative (WRHI) of Tokyo Institute of Technology.

References

1 G. A. Jeffrey and W. Saenger, *Hydrogen Bonding in Biological Structures*, Sprinter-Verlag, 1991.
2 T. S. Zwier, *Annu. Rev. Phys. Chem.*, 1996, **47**, 205–241.
3 K. Müller-Dethlefs and P. Hobza, *Chemical Reviews*, 2000, **100**, 143–168.
4 C. E. H. Dessent and K. Müller-Dethlefs, *Chem. Rev.*, 2000, **100**, 3999–4022.
5 J. Schermann, *Spectroscopy and Modelling of Biomolecular Building Blocks*, Elsevier, 2008.
6 P. Hobza and K. Müller-Dethlefs, *Non-Covalent Interactions*, The Royal Society of Chemistry, 2009, pp. P001–P226.
7 K. Mizuse and A. Fujii, *Int. Rev. Phys. Chem.*, 2013, **32**, 266–307.
8 G. Otting, E. Liepinsh and K. Wuthrich, *Science*, 1991, **254**, 974–980.
9 V. Denisov, B.-H. Jonsson and B. Halle, *Nat. Struct. Mol. Biol.*, 1999, **6**, 253–260.
10 *Mechanisms of Protein Folding*, ed. R. H. Pain, Oxford University Press, 2000.
11 A. Mitsutake, Y. Sugita and Y. Okamoto, *Peptide Science*, 2001, **60**, 96–123.
12 N. Nucci, M. Pometun and A. Wand, *Nat. Struct. Mol. Biol.*, 2011, **18**, 245–249.
13 S. K. Pal and A. H. Zewail, *Chem. Rev.*, 2004, **104**, 2099–2124.
14 B. Halle, *Philos. Trans. R. Soc. London Ser. B*, 2004, **359**, 1207–1224.
15 B. Bagchi, *Chem. Rev.*, 2005, **105**, 3197–3219.
16 D. Chandler, *Nature*, 2005, **437**, 640–647.
17 M. Chaplin, *Nat. Rev. Mol. Cell. Biol.*, 2006, **7**, 861–866.
18 P. Ball, *Chem. Rev.*, 2008, **108**, 74–108.
19 D. Zhong, *Adv. Chem. Phys.*, 2009, **143**, 83–149.
20 D. E. Shaw, P. Maragakis, K. Lindorff-Larsen, S. Piana, R. O.

Dror, M. P. Eastwood, J. A. Bank, J. M. Jumper, J. K. Salmon, Y. Shan and W. Wriggers, *Science*, 2010, **330**, 341–346.
21 T. Yoda, Y. Sugita and Y. Okamoto, *Biophys. J*, 2010, **99**, 1637–1644.
22 M. Grossman, B. Born, M. Heyden, D. Tworowski, G. Fields, I. Sagi and M. Havenith, *Nat. Struct. Mol. Biol.*, 2011, **18**, 1102–1108.
23 S. Kalko, E. Guardia and J. Padro, *J. Phys. Chem. B*, 1999, **103**, 3935–3941.
24 A. C. Fogarty, E. Duboue-Dijon, F. Sterpone, J. T. Hynes and D. Laage, *Chem. Soc. Rev.*, 2013, **42**, 5672–5683.
25 O. Dopfer and M. Fujii, *Chem. Rev.*, 2016, **116**, 5432–5463.
26 D. M. Neumark, *Annu. Rev. Phys. Chem.*, 2001, **52**, 255–277.
27 A. Stolow, A. E. Bragg and D. M. Neumark, *Chem. Rev.*, 2004, **104**, 1719–1758.
28 T. Suzuki, *Annu. Rev. Phys. Chem.*, 2006, **57**, 555–592.
29 A. Stolow and J. G. Underwood, in *Time-Resolved Photoelectron Spectroscopy of Nonadiabatic Dynamics in Polyatomic Molecules*, ed. S. A. Rice, John Wiley & Sons, Inc., 2008, pp. 497–584.
30 M. Fujii and O. Dopfer, *Int. Rev. Phys. Chem.*, 2012, **31**, 131–173.
31 S. Ishiuchi, M. Sakai, Y. Tsuchida, A. Takeda, Y. Kawashima, M. Fujii, O. Dopfer and K. Müller-Dethlefs, *Angew. Chem. Int. Ed.*, 2005, **44**, 6149–6151.
32 M. Miyazaki, A. Takeda, S. Ishiuchi, M. Sakai, O. Dopfer and M. Fujii, *Phys. Chem. Chem. Phys.*, 2011, **13**, 2744–2747.
33 S. Ishiuchi, M. Miyazaki, M. Sakai, M. Fujii, M. Schmies and O. Dopfer, *Phys. Chem. Chem. Phys.*, 2011, **13**, 2409–2416.
34 M. Miyazaki, Y. Sakata, M. Schütz, O. Dopfer and M. Fujii, *Phys. Chem. Chem. Phys.*, 2016, **18**, 24746–24754.
35 M. Miyazaki, T. Nakamura, M. Wohlgemuth, R. Mitrić, O. Dopfer and M. Fujii, *Phys. Chem. Chem. Phys.*, 2015, **17**, 29969–29977.
36 K. Tanabe, M. Miyazaki, M. Schmies, A. Patzer, M. Schütz, H. Sekiya, M. Sakai, O. Dopfer and M. Fujii, *Angew. Chem. Int. Ed.*, 2012, **124**, 6708–6711.
37 M. Wohlgemuth, M. Miyazaki, M. Weiler, M. Sakai, O. Dopfer, M. Fujii and R. Mitrić, *Angew. Chem. Int. Ed.*, 2014, **53**, 14601–14604.
38 C. A. Lipinski, F. Lombardo, B. W. Dominy and P. J. Feeney, *Adv. Drug Deliv. Rev.*, 1997, **23**, 3 – 25.
39 J. Chatterjee, C. Gilon, A. Hoffman and H. Kessler, *Acc. Chem. Res.*, 2008, **41**, 1331–1342.
40 N. Qvit, S. J. Rubin, T. J. Urban, D. Mochly-Rosen and E. R. Gross, *Drug Discov. Today*, 2017, **22**, 454 – 462.
41 E. G. Robertson, *Chem. Phys. Lett.*, 2000, **325**, 299–307.
42 T. Ikeda, K. Sakota, Y. Kawashima, Y. Shimazaki and H. Sekiya, *J. Phys. Chem. A*, 2012, **116**, 3816–3823.
43 J. R. Clarkson, E. Baquero, V. A. Shubert, E. M. Myshakin, K. D. Jordan and T. S. Zwier, *Science*, 2005, **307**, 1443–1446.
44 S. Ullrich, X. Tong, G. Tarczay, C. E. H. Dessent and K. Müller-Detlefs, *Phys. Chem. Chem. Phys.*, 2002, **4**, 2897–2903.
45 M. Sakota, Y. Shimazaki and H. Sekiya, *Phys. Chem. Chem. Phys.*, 2011, **13**, 6411–6415.
46 J. Klyne, M. Schmies, M. Fujii and O. Dopfer, *J. Phys. Chem. B*, 2015, **119**, 1388–1406.
47 H. Tachikawa, M. Igarashi and T. Ishibashi, *J. Phys. Chem. A*, 2003, **107**, 7505–7513.
48 J. Klyne, M. Schmies and O. Dopfer, *J. Phys. Chem. B*, 2014, **118**, 3005–3017.
49 V. Bonačić-Koutecký and R. Mitrić, *Chem. Rev.*, 2005, **105**, 11–66.
50 R. Mitrić and V. Bonačić-Koutecký, *Phys. Rev. A*, 2007, **76**, 031405.
51 S. Ishiuchi, M. Sakai, Y. Tsuchida, A. Takeda, Y. Kawashima, O. Dopfer, K. Müller-Dethlefs and M. Fujii, *J. Chem. Phys.*, 2007, **127**, 114307.
52 S. Ishiuchi, M. Sakai, K. Daigoku, K. Hashimoto and M. Fujii, *J. Chem. Phys.*, 2007, **127**, 234304.
53 J. A. Dickinson, M. R. Hockridge, E. G. Robertson and J. P. Simons, *J. Phys. Chem. A*, 1999, **103**, 6938–6949.
54 A. Fedorov and J. R. Cable, *J. Phys. Chem. A*, 2000, **104**, 4943.
55 M. Mons, I. Dimicoli, B. Tardivel, F. Piuzzi, E. G. Robertson and J. P. Simons, *J. Phys. Chem. A*, 2001, **105**, 969–973.
56 T. Omi, H. Shitomi, N. Sekiya, K. Takazawa and M. Fujii, *Chem. Phys. Lett.*, 1996, **252**, 287–293.
57 J. Perdew and Y. Wang, *Phys. Rev. B*, 1992, **45**, 13244.
58 J. Perdew, K. Burke and M. Ernzerhof, *Phys. Rev. Lett.*, 1996, **77**, 3865.
59 *TURBOMOLE V6.2 2010, a development of University of Karlsruhe and Forschungszentrum Karlsruhe GmbH, 1989-2007, TURBOMOLE GmbH, since 2007; available from* `http://www.turbomole.com`.
60 T. Y. D. Tew and N. Handy, *Chem. Phys. Lett.*, 2004, **393**, 51–57.
61 M. J. Frisch, G. W. Trucks, H. B. Schlegel, G. E. Scuseria, M. A. Robb, J. R. Cheeseman, G. Scalmani, V. Barone, B. Mennucci, G. A. Petersson, H. Nakatsuji, M. Caricato, X. Li, H. P. Hratchian, A. F. Izmaylov, J. Bloino, G. Zheng, J. L. Sonnenberg, M. Hada, M. Ehara, K. Toyota, R. Fukuda, J. Hasegawa, M. Ishida, T. Nakajima, Y. Honda, O. Kitao, H. Nakai, T. Vreven, J. J. A. Montgomery, J. E. Peralta, F. Ogliaro, M. Bearpark, J. J. Heyd, E. Brothers, K. N. Kudin, V. N. Staroverov, R. Kobayashi, J. Normand, K. Raghavachari, A. Rendell, J. C. Burant, S. S. Iyengar, J. Tomasi, M. Cossi, N. Rega, J. M. Millam, M. Klene, J. E. Knox, J. B. Cross, V. Bakken, C. Adamo, J. Jaramillo, R. Gomperts, R. E. Stratmann, O. Yazyev, A. J. Austin, R. Cammi, C. Pomelli, J. W. Ochterski, R. L. Martin, K. Morokuma, V. G. Zakrzewski, G. A. Voth, P. Salvador, J. J. Dannenberg, S. Dapprich, A. D. Daniels, Ö. Farkas, J. B. Foresman, J. V. Ortiz, J. Cioslowski and D. J. Fox, *Gaussian 09 Revision E.01*, Gaussian Inc. Wallingford CT 2009.
62 R. Krishnan, J. Binkley, R. Seeger and J. Pople, *J. Chem. Phys.*, 1980, **72**, 620.
63 S. Grimme, *J. Comput. Chem.*, 2004, **25**, 1463–1473.
64 W. C. Swope, H. C. Andersen, P. H. Berens and K. R. Wilson,

J. Chem. Phys., 1982, **76**, 637.
65 K. Sakota, S. Harada, Y. Shimazaki and H. Sekiya, *J. Phys. Chem. A*, 2011, **115**, 626–630.
66 S. Ullrich and K. Müller-Dethlefs, *J. Phys. Chem. A*, 2002, **106**, 9188–9195.